Two Wide-Angle Imaging Neutral-Atom Spectrometers and Interstellar Boundary Explorer energetic neutral atom imaging of the 5 April 2010 substorm

D. J. McComas,[1,2] N. Buzulukova,[3,4] M. G. Connors,[5,6] M. A. Dayeh,[1] J. Goldstein,[1,2] H. O. Funsten,[7] S. Fuselier,[1] N. A. Schwadron,[8,9] and P. Valek[1,2]

Received 17 October 2011; revised 28 December 2011; accepted 1 February 2012; published 27 March 2012.

[1] This study is the first to combine energetic neutral atom (ENA) observations from Two Wide-Angle Imaging Neutral-Atom Spectrometers (TWINS) and Interstellar Boundary Explorer (IBEX). Here we examine the arrival of an interplanetary shock and the subsequent geomagnetically effective substorm on 5 April 2010, which was associated with the Galaxy 15 communications satellite anomaly. IBEX shows sharply enhanced ENA emissions immediately upon compression of the dayside magnetosphere at 08:26:17+/−9 s UT. The compression drove a markedly different spectral shape for the dayside emissions, with a strong enhancement at energies >1 keV, which persisted for hours after the shock arrival, consistent with the higher solar wind speed, density, and dynamic pressure ($\sim$10 nPa) after the shock. TWINS ENA observations indicate a slower response of the ring current and precipitation of ring current ions as low-altitude emissions $\sim$15 min later, with the >50 keV ion precipitation leading the <10 keV precipitation by $\sim$20 min. These observations suggest internal magnetospheric processes are occurring after compression of the magnetosphere and before the ring current ions end up in the loss cone and precipitate into the ionosphere. We also compare MHD simulation results with both the TWINS and IBEX ENA observations; while the overall fluxes and distributions of emissions were generally similar, there were significant quantitative differences. Such differences emphasize the complexity of the magnetospheric system and importance of the global perspective for macroscopic magnetospheric studies. Finally, Appendix A documents important details of the TWINS data processing, including improved binning procedures, smoothing of images to a given level of statistical accuracy, and differential background subtraction.

Citation: McComas, D. J., N. Buzulukova, M. G. Connors, M. A. Dayeh, J. Goldstein, H. O. Funsten, S. Fuselier, N. A. Schwadron, and P. Valek (2012), Two Wide-Angle Imaging Neutral-Atom Spectrometers and Interstellar Boundary Explorer energetic neutral atom imaging of the 5 April 2010 substorm, *J. Geophys. Res.*, *117*, A03225, doi:10.1029/2011JA017273.

1. Introduction

[2] Intelsat's Galaxy 15 communications satellite in geosynchronous orbit experienced anomalies leading to loss of control at 09:48 UTC on 5 April 2010. This event correlated with disturbed space weather conditions associated with a coronal mass ejection (CME) driven shock that impacted and compressed the Earth's magnetosphere at approximately 08:25 UT on that day [*Singer et al.*, 2010]. After loss of command and control, the satellite began drifting away from its allotted geosynchronous location and with the potential to disrupt the missions of nearby satellites through frequency interference. Fortunately, operators were ultimately able to restore control and, after nearly a year of lost capability, on 18 March 2011 Galaxy 15 was recertified and was repositioned back near its original location in early April 2011.

[3] The magnetospheric events of 5–7 April 2010 were driven by a fast coronal mass ejection (CME) that was directly observed by the STEREO spacecraft to leave the

[1]Southwest Research Institute, San Antonio, Texas, USA.
[2]Department of Physics and Astronomy, University of Texas at San Antonio, San Antonio, Texas, USA.
[3]CRESST and Geospace Physics Laboratory, NASA Goddard Space Flight Center, Greenbelt, Maryland, USA.
[4]Department of Astronomy, University of Maryland, College Park, Maryland, USA.
[5]Department of Physics and Astronomy, Athabasca University Geophysical Observatory, Athabasca University, Athabasca, Alberta, Canada.
[6]Department of Earth and Space Sciences, University of California, Los Angeles, California, USA.
[7]Los Alamos National Laboratory, Los Alamos, New Mexico, USA.
[8]Department of Physics, University of New Hampshire, Durham, New Hampshire, USA.
[9]Also at Southwest Research Institute, San Antonio, Texas, USA.

0148-0227/12/2011JA017273

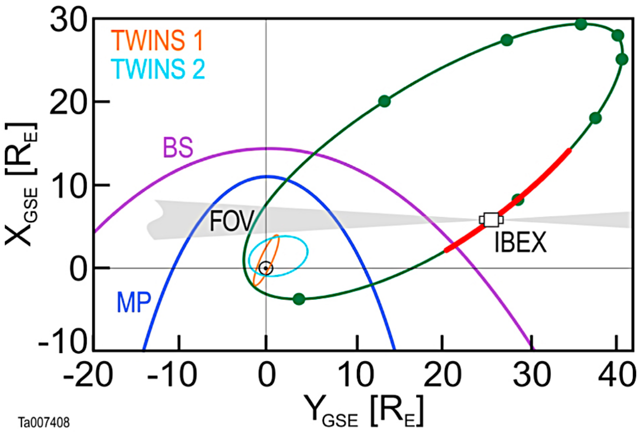

Figure 1. Plot of the IBEX and TWINS orbits in the GSE *X-Y* plane. IBEX orbits nearly in this plane, and dots along its orbit indicate 1 day intervals with the red segment identifying all of 5 April 2010. The IBEX spacecraft has a 7° FWHM FOV (gray) that was repeatedly scanning across the dayside magnetosphere on this day as IBEX moved counterclockwise along its orbit. TWINS 1 and 2 are in Molniya orbits, which are highly inclined to the Earth's equator, leading to the different apparent shapes in this plot, and have geocentric apogees >7 R_E, so that the bulk of the orbit extends out of the page.

Sun on 3 April [*Möstl et al.*, 2010]. The initial interaction began with the CME-driven shock that arrived at Earth at ~08:25 UT on 5 April. *Connors et al.* [2011] examined multiple in situ observations of this event, including the magnetospheric response measured at THEMIS A, D, and E, which were near each other in the northern plasma sheet in the early morning sector, and GOES 11, which was near magnetic midnight. At the time, Geotail was ~14.7 R_E upstream of the Earth near the Earth-Sun line, and thus made direct observations of the solar wind that only required ~100 s delay in order to translate them to the magnetopause. Because there was only a very limited duration of southward IMF, the resulting magnetospheric storm was small [*Möstl et al.*, 2010]. However, this limited but strong southward field and high solar wind dynamic pressure immediately following the CME shock led to the interesting substorm examined here.

[4] *Connors et al.*'s [2011] interpretation of this event was that a substorm growth phase was followed by strong flux transfer to the inner magnetosphere, producing "over-dipolarization" in the midnight sector. They used multiple in situ and ground-based observations to show that the flux transfer was consistent with a substorm current wedge and provided perhaps the most complete set of geophysical signatures supporting the near-Earth, neutral-line interpretation of substorms. *Connors et al.* [2011] also argued that the location of Galaxy 15 near midnight subjected it to extreme space weather conditions, suggesting that they were causative in disruption of its operation.

[5] In contrast to and augmenting these detailed multipoint in situ observations, this study is the first ever to combine simultaneous energetic neutral atom (ENA) imaging observations from two separate missions with quite different vantage points. Here, we examine the global aspects and timing of the unusual magnetospheric events on 5 April 2010 using remote observations from the Two Wide-Angle Imaging Neutral-Atom Spectrometers (TWINS) [*McComas et al.*, 2009a] and Interstellar Boundary Explorer (IBEX) [*McComas et al.*, 2009b] missions. The unprecedented combination of IBEX and TWINS provides simultaneous observations of internal and external magnetospheric processes, which yields a new connected view of the perturbed magnetosphere.

[6] The TWINS mission [*McComas et al.*, 2009a] was designed to extend our understanding of magnetospheric structure and processes by stereoscopically imaging the Earth's magnetosphere from two locations for the first time. TWINS began making stereo ENA images of the magnetosphere over energies from 1 to 100 keV with high angular (~4° × 4°) resolution, in June 2008. These observations have continued through the deepest solar minimum of the space age and, in spite of the geomagnetically quiet times, TWINS observations are contributing importantly to the understanding of numerous magnetospheric phenomena, including (1) small storms (minimum Dst ~ −70) [*Valek et al.*, 2010], (2) bright low-altitude emissions, from precipitating ring current ions [e.g., *Bazell et al.*, 2010], (3) the spatial distribution of plasma sheet temperatures [*Keesee et al.*, 2011], (4) inversions of magnetospheric ion distributions [*Grimes et al.*, 2010], and (5) detailed comparisons with global magnetospheric simulations such as the CRCM [e.g., *Buzulukova et al.*, 2010].

[7] In contrast to TWINS, IBEX was designed to use ENAs to make the first observations of the interaction of our heliosphere with the local interstellar medium [*McComas et al.*, 2009c, 2011a]. While far exceeding expectations in this arena, IBEX has also proven to be an outstanding mission for observing the Earth's magnetosphere from the outside, already showing emissions from the stagnation region ahead of the nose of the magnetopause [*Fuselier et al.*, 2010], the plasma sheet in the Earth's magnetotail, including observations of a possible plasma sheet disconnection event [*McComas et al.*, 2011b], and asymmetric ENA emissions from the magnetospheric cusps [*Petrinec et al.*, 2011].

2. Observations

[8] The geometry of the IBEX and TWINS spacecraft on 5 April 2010 is shown in Figure 1; IBEX's orbit is roughly in the GSE Z = 0 plane (shown). The heavy red portion of this orbit indicates the motion of IBEX over the full day of 5 April. Because IBEX is a nearly Sun-pointed 4 rpm spinner (15 s period), its 7° full width at half maximum (FWHM) field of view (FOV) observes a broad cut across the dayside magnetosphere throughout this entire day. As time progresses, IBEX moves slowly (counterclockwise) along its orbit and views progressively further ahead of the Earth. While not well suited for imaging the X extent of emitting structures, these observations are ideal for measurements of timing, Z extent, flux variations, and energy spectral changes from a broad dayside emission region.

[9] The TWINS spacecraft are in Molniya orbits, with inclinations of 63.4°, apogees of ~7.2 R_E geocentric, and orbital periods of precisely one half of a sidereal day. At ~08:30 UT on 5 April 2010, the respective approximate

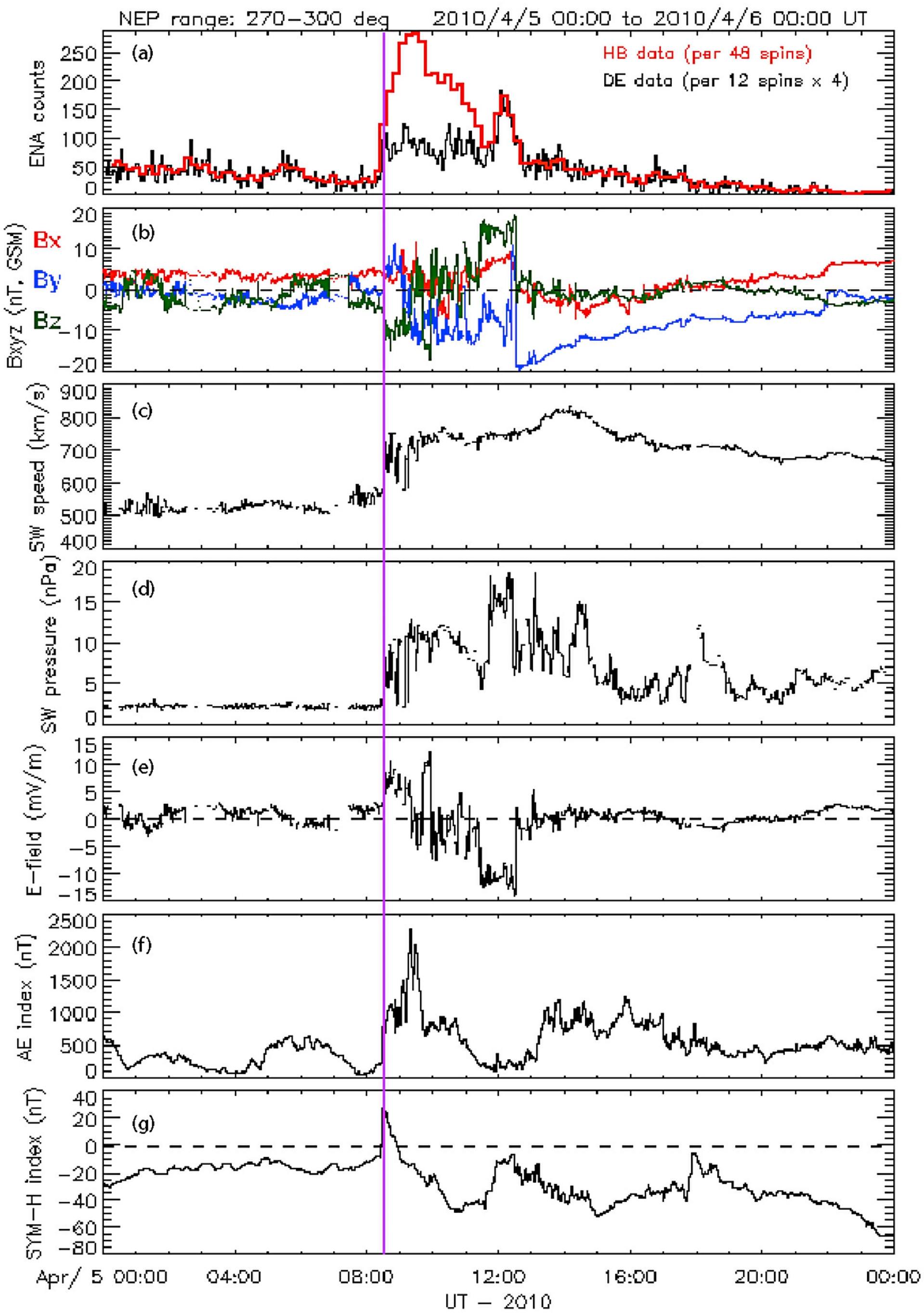

Figure 2. ENA counts in ESA step 5 are shown along with solar wind parameters taken from the ACE/Wind spacecraft propagated to the magnetosphere as a part of the OMNI data set and geomagnetic indices for all of 5 April 2010: (a) ENA counts in ESA step 5, (b) interplanetary magnetic field, (c) solar wind (sw) speed, (d) solar wind dynamic pressure, (e) solar wind motional electric field, and (f and g) geomagnetic responses *AE* and *SYM-H.* The interplanetary shock arrived at ~08:25 UT (vertical line). HB, histogram binned; DE, direct event.

local times of TWINS 1 and TWINS 2 are ~19:30 and 09:20. The TWINS spacecraft are spaced and phased in their orbits so that the ENA imagers provide nearly continuous magnetospheric observations throughout the day with simultaneous, stereo imaging for over an hour centered roughly on 06:00, 12:00, 18:00, and 24:00 UT. The combination of IBEX and TWINS observations allows for the first ever three-point ENA imaging of the magnetosphere (or in fact, any space plasma).

[10] Figure 2 summarizes the ENA emissions observed by IBEX (Figure 2a), solar wind parameters taken from the ACE/Wind spacecraft propagated to the magnetosphere by OMNI (Figures 2b–2e), and geomagnetic response (Figures 2f and 2g) for all of 5 April 2010. The interplanetary

Table 1. IBEX-Hi Energy Bands and Approximate Observational Time Lags

ESA Level	E_{Nom} −FWHM (keV)	E_{Nom} (keV)	E_{Nom} +FWHM (keV)	Speed of H at E_{Nom} (km/s)	27 R_E Travel Time (s)	Arrival After Energy Step 6 (s)
1	0.38	0.45	0.58	293.5	587	392
2	0.52	0.71	0.95	368.7	467	272
3	0.84	1.08	1.55	454.7	379	184
4	1.36	1.85	2.50	595.2	290	95
5	1.99	2.70	3.75	719.0	240	45
6	3.13	4.09	6.00	885.0	195	0

shock arrived at the magnetosphere at ~08:25 UT. B_Z (green in Figure 2b) varied between slightly positive and slightly negative for the hours leading up the shock and then turned quickly southward ($B_Z \sim -13$ nT), continuing for more than an hour after the shock arrival; this southward field and a jump in the solar wind flow speed (Figure 2c) from ~550 km s^{-1} to ~700 km s^{-1}, created a substantial motional electric field (Figure 2e) coupled into the magnetosphere. Furthermore, the increased speed (Figure 2c) and density (not shown) caused the solar wind ram pressure (Figure 2d) to jump from ~2 to ~10 nPa, likely causing a significant compression of the overall magnetosphere. In addition, while both the density and temperature (not shown) are elevated after the passage of the interplanetary shock, the ENA emissions seemingly track the density profile (especially the enhancement at ~12:00 UT), suggesting that enhanced ENA emissions are, not surprisingly, directly related to the density of the source ions. The *AE* (Figure 2f) and *SYM-H* (Figure 2g) geomagnetic indices responded essentially instantaneously with jumps across the shock arrival of ~200 to 800 and ~−10 to +20, respectively.

[11] Figure 2a shows the ENA counts observed in the IBEX-Hi energy step 5, which measures 1.99–3.75 keV (FWHM) H ENAs (note that IBEX's detection efficiency for heavier ENAs is extremely low). IBEX acquires ENA data in each of six energy steps (see Table 1) by stepping up every two spins (i.e., the sequence of energy steps on subsequent spins is 1,1,2,2,3,3,4,4,5,5,6,6,1,1…). Thus, the fundamental time resolution for a single sample at any given energy is 15 s, but only two of these are taken sequentially at each of six energy steps, so that the full cycle repeats every ~3 min. The red curve in Figure 2a shows histogram-binned (HB) data that are summed onboard over 48 spins (~12 min); because of the sampling sequence, this observation consists of ~2 min of data collection time for energy step 5 sampled in eight segments over ~12 min. The black curve shows direct event (DE) data from each pair of spins at this energy step (taken on a pair of spins each 12 spins) where we have multiplied the observed counts by 48/12 in order to put both curves on the same scale. Note that the two curves match for times of lower count rates, but for higher counts, the direct events undersample the ENAs owing to IBEX's limited telemetry rates. This by-design combination allows us to use direct event data for more accurate timing, while the histogram data of all ENAs (summed onboard) provide accurate fluxes at somewhat lower time resolution.

[12] ENA emissions from the dayside magnetosphere are shown in Figure 3. The two intervals represent the ~3 h before the shock arrival (Figures 3a and 3c) and the ~1 h after (Figures 3b and 3d); Figures 3a and 3b are based on histogram data for energy step 3 (~1.1 keV), and the bottom shows energy step 5 (~2.7 keV). In contrast to the direct events, the histogram data capture all ENAs measured at these energies by IBEX. The preshock images (Figures 3a and 3c) show ENA emissions from both magnetospheric cusps as described by *Petrinec et al.* [2011]; it is interesting to note that there are higher ENA emissions from the southern cusp than from the northern cusp prior to the interplanetary shock arrival that seem to disappear after arrival. After the shock arrives at Earth (Figures 3b and 3d), the magnetopause is likely compressed, and IBEX observes strongly enhanced emissions from the nose of the magnetosphere and magnetosheath, as examined by *Fuselier et al.* [2010].

[13] Figure 4a again shows the ENA counts measured in ESA 5 from 07:00 to 16:00 UT. Six sequential intervals (I–VI) are identified and color coded. The energy spectra for all six intervals are plotted in Figure 4b, with both the spectra and their time ranges indicated by the color coding. Clearly the preshock cusp emissions (I, black) are very different from the post shock, compressed magnetosheath emissions (II–VI). In particular, even in the initial ramping up of the ENA emissions (II, red), their spectrum is strongly enhanced at energies >1 keV compared to lower energies. This higher-energy enhancement grows even stronger through the peak ENA fluxes (III, yellow) and then slightly lessens through the remainder of the enhanced fluxes (IV, green and V, light blue). By the end of the interval examined (VI, dark blue), the lower-energy fluxes have dropped back essentially to their preshock levels, while the higher-energy fluxes remain significantly enhanced. This sequence of observations begs the question as to why the peak energy is as low as it is and whether the solar wind or magnetosheath plasma ions are producing the bulk of the observed ENAs.

[14] Because IBEX was designed to measure the tenuous ENA emissions from the outer heliosphere, the sensors were optimized to provide extremely high sensitivity. This sensitivity allows very precise observations such as the spectral information shown in Figure 4, even when the ENA source is far from the Earth, where the neutral exospheric densities, with which the ions charge exchange, are extremely low. It also provides adequate statistics of measurements from these distant regions to allow reasonably precise timing of significant changes in magnetospheric emissions. Figure 2a shows ENA counts in 12 spins (~3 min), which clearly show a discontinuous enhancement just prior to 08:30 UT. In addition, we examined IBEX's individual direct event data from individual spins at each of the six observed energies. These pass bands collectively span from 0.38–6.00 keV FWHM and have different transit times for the different speed ENAs, as shown in Table 1, from the emission region near the nose of the magnetopause ~27 R_E away.

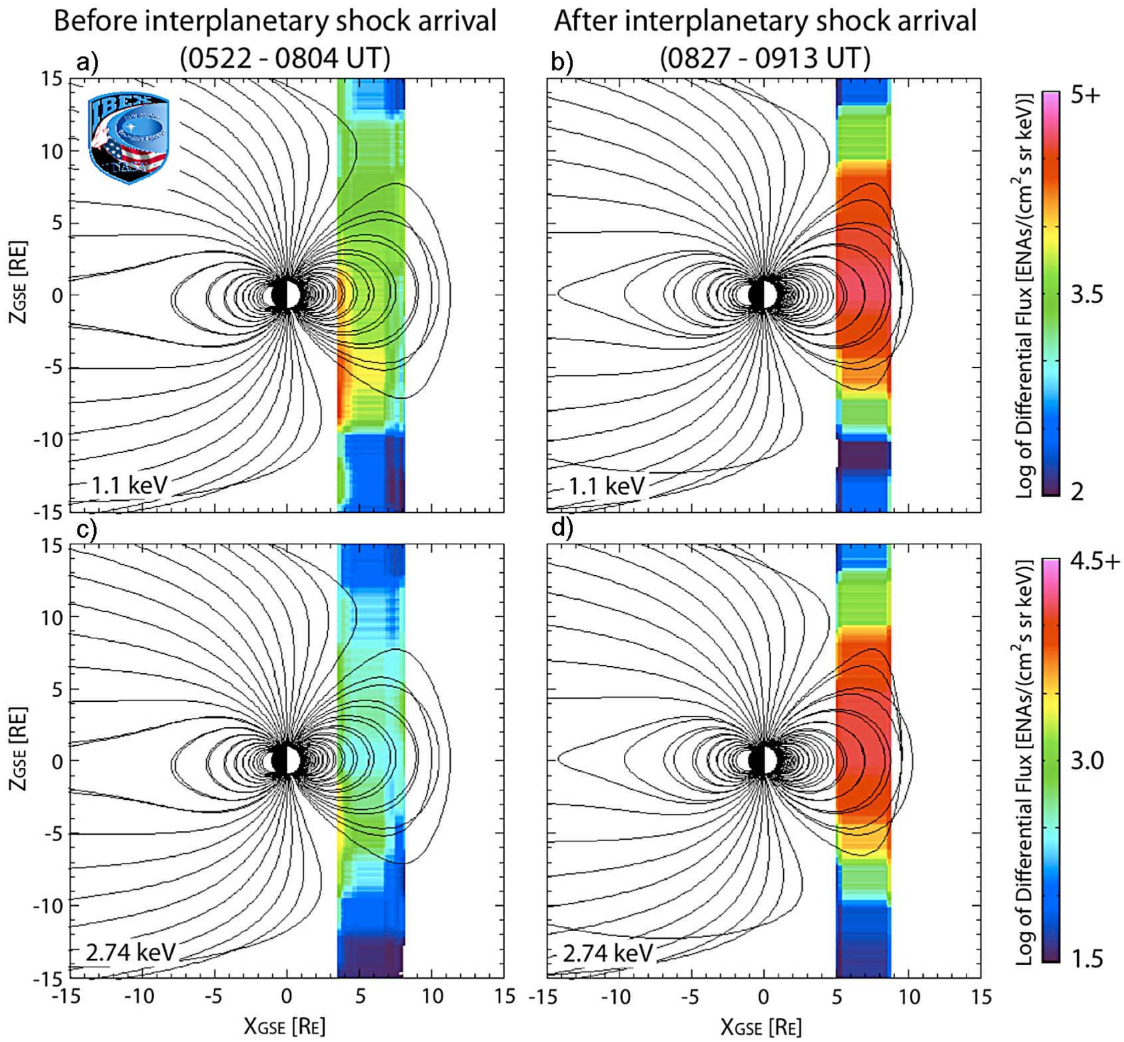

Figure 3. IBEX images of differential flux of ENAs observed from the dayside of the Earth for energy bands centered on (a and b) 1.1 keV and (c and d) 2.7 keV. Figures 3a and 3c show times before the interplanetary shock arrival (05:22–08:04 UT), and Figures 3b and 3d show those after (08:27–09:13). Images are constructed from the combination of spinning and motion of the IBEX spacecraft along its orbit over the interval integration interval; this, along with IBEX's intrinsic ~7° FWHM angular resolution, produces the blocky ENA features shown [e.g., *McComas et al.*, 2011b]. The modeled magnetic field lines [*Tsyganenko*, 1995] are calculated for the central time in the ENA observation interval shown in each image and projected onto the GSE *X-Z* plane; the model field in Figures 3b and 3d probably shows less compression than actually occurred, and the bright ENA emissions are likely coming at least in part from the highly compressed subsolar magnetosheath.

[15] While the counting statistics are limited in the individual spin data, discontinuous jumps can be seen in each of the six energy steps with generally later times at progressively lower energies as expected for the transit time delays. The last three columns of Table 1 show the speed of an H ENA at the central energy of each energy step, the transit time for the ENA to propagate from the nose of the magnetosphere to IBEX (~27 R_E), and the differential time lag from the fastest ENAs observed. In Figure 5, we show a dispersion analysis of the timing of the onset of enhanced ENA fluxes. For each energy bin, the vertical bars indicate the range of possible arrival times with the lower ends corresponding to the measurements just before the enhancement and the upper ends the measurements just after. Horizontal bars indicate the FWHM ranges of the six energy channels (Table 1). The distance to the source determines a fixed slope in 1/v versus time; here we assume that the enhancement begins at the distance to the GSE *x* axis (27 R_E), where the nose of the magnetosphere should first encounter the interplanetary shock arrival. For this distance, the initial ENA enhancement must have started between 08:26:08 and 08:26:26 UT, bounded by the earliest time for ESA 5 (blue dot) and the latest time for ESA 2 (red dot), in order to account for the increases seen at all energies.

[16] Measurements of ENAs from near the nose of the magnetopause provide a global view of conditions in this region [*Fuselier et al.*, 2010]. As such, they allow a global (although integrated) test of results from global

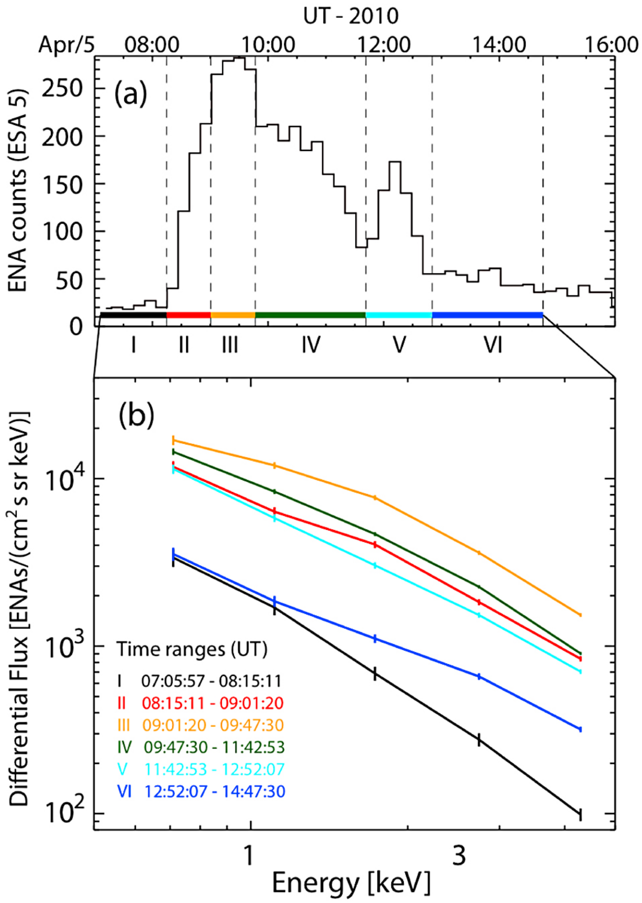

Figure 4. (a) ENA counts in ESA 5, color coded to provide a guide to the ENA energy spectra measured by IBEX. (b) Energy spectra from before the shock arrival (black) through the substorm. Error bars represent $\pm 1\sigma$ Poisson statistical errors (square root of the counts).

magnetospheric magnetohydrodynamic (MHD) simulations of this region. MHD results at any point in a model are characterized by the magnetic field, density, temperature, and plasma velocity. The distribution function may be characterized by a drifting Maxwellian, and in turn the relevant differential directional intensity as a function of particle energy E [*Rossi and Olbert*, 1970] may be found as

$$J_{ion}(E,\vec{v},\vec{x}) = \frac{v^2}{m} f(\vec{v},\vec{x}) = \frac{v^2}{m} n \left(\frac{m}{2\pi kT}\right)^{3/2} \exp\left(-\frac{m(\vec{v}-\vec{v}_0)^2}{2kT}\right), \quad (1)$$

where $\mathbf{v}$ is from the emission point $\mathbf{x}$ toward the observation point, n is the particle density, T is the temperature, and $\mathbf{v}_0$ is the plasma bulk velocity. The ENA brightness at the spacecraft is obtained by integrating the optically thin ENA emissions along each line of sight,

$$J_{ENA}(E,x,z) = \int J_{ion}(E,x,y,z)\,\sigma(E)\,n_H(x,y,z)\,dy, \quad (2)$$

where σ is the cross section for energetic protons scattering from neutral hydrogen of the geocorona, whose particle density is n_H. In order to compare directly the modeled ENA intensities with the IBEX data shown in Figure 3, we performed the integral here along GSE Y, giving a map of ENA emission as a function of GSE X and Z, consistent with the image plane observed by IBEX for this event.

[17] We ran the Open Geospace General Circulation Model (Open GGCM) [*Raeder et al.*, 2001] at the Community Coordinated Modeling Center using propagated solar wind input for the day of 5 April 2010. We downloaded physical quantities from this model on a one R_E grid and interpolated in three dimensions. We also used the empirical geocoronal density model from *Rairden et al.* [1986]. Since the charge exchange cross section [*Lindsay and Stebbings*, 2005] is relatively constant across the energy range considered, we used a constant value of $\sigma = 2 \times 10^{-15}$ cm^2 and approximated the energy response of the detector as flat across the energy band half widths given in Table 1. We used a fixed IBEX position of (6,25,0) R_E in GSE coordinates throughout the event. For comparison with Figure 3, it is necessary to average model results in time to compare with the IBEX exposures over similar time periods. Over the less dynamic and longer early period of observation, we averaged model values from 06:04 to 08:04 UT at 20 min intervals, while in the dynamic period 08:28 to 09:12 UT we averaged over 4 min intervals, to calculate the projected ENA emissions. Dynamics visible in individual steps of the model simulations are not examined here, but the averaging produced images directly comparable to the IBEX observations over the matching time periods.

[18] The results in Figure 6 show general agreement of the model with the IBEX observations in terms of integrated brightness at ~2.7 keV from around the nose of the magnetopause after the interplanetary shock arrival. Simulated fluxes in this energy band from before the shock and at ~1.1 keV both before and after the shock arrival are significantly different from the observations, with the model showing relatively little intensification at ~1.1 keV arrival compared to the observations. In addition, a discrete feature above the Z = 0 plane at about X = 7 R_E is evident before the

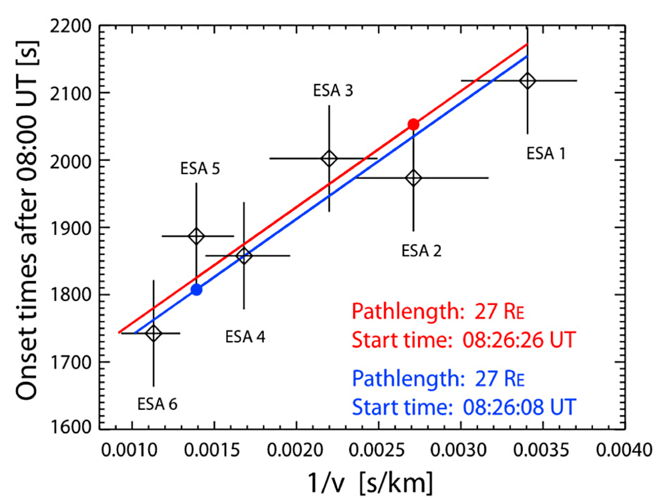

Figure 5. ENA dispersion analysis for initial enhancement times seen in each of the six IBEX-Hi energy channels. For a source at the nose of the magnetopause, 27 R_E away, the initial ENA intensification must have occurred between 08:26:08 and 08:26:26 UT.

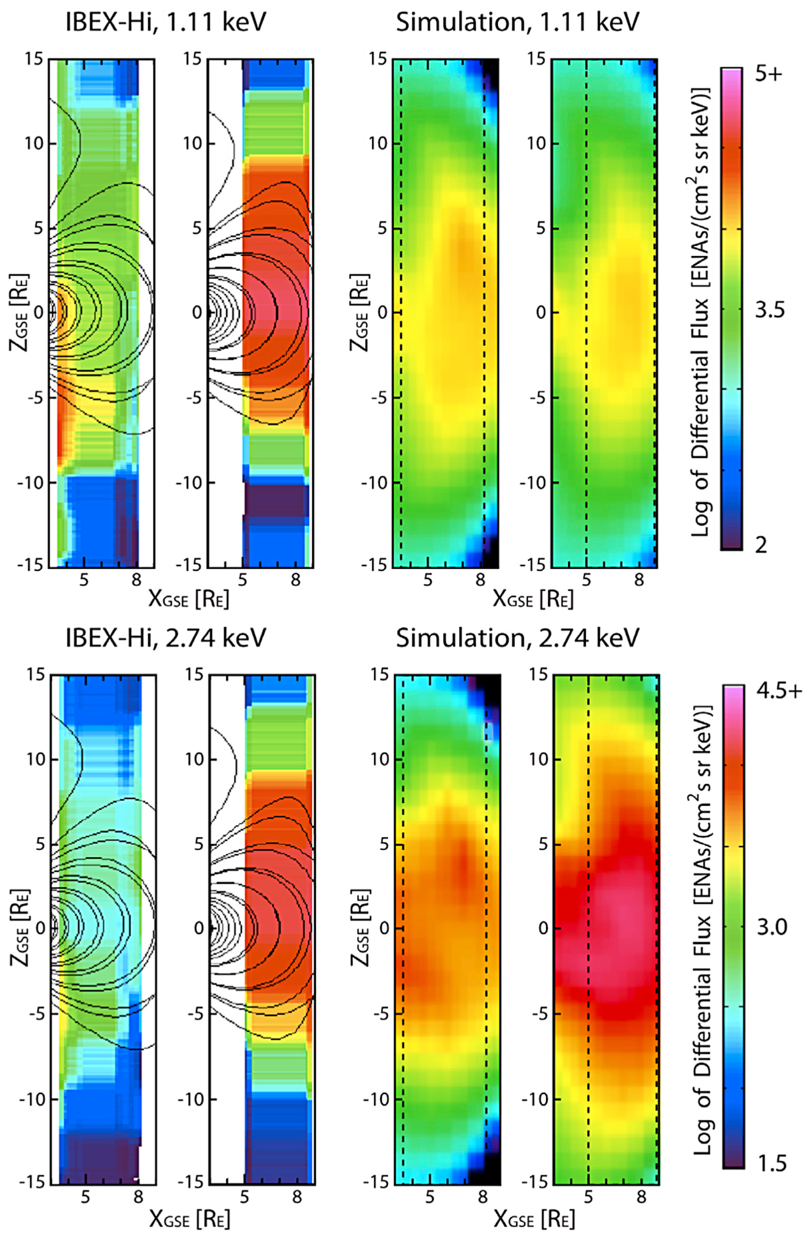

Figure 6. Comparison of (left) ENA observations from Figure 3 with (right) simulated ENA emissions using the same color bars. The left (right) image in each pair shows emissions before (after) the arrival of the interplanetary shock, the top images are all for ESA 3 (1.1 keV central energy), and the bottom images are for ESA 5 (2.7 keV central energy).

shock arrival in the simulated image but not in the observations. The model showed considerable dynamical behavior in the earlier period, which corresponded to a period of elevated *AE* (see Figure 2). The model's discrete features at ~1.1 keV (visible to a lesser extent at the higher energy), and overall brightness in the earlier period in ESA 3, appear to be due to plasma flows present in the model, which the IBEX observations do not provide evidence of. In contrast, the model does not show enhanced cusp emissions [*Petrinec et al.*, 2011] as clearly seen in the IBEX observations.

[19] While derivation of emission intensities from inner magnetospheric models has been done before [*Fok et al.*, 2003; *Lee et al.*, 2007; *Buzulukova et al.*, 2010], IBEX also detects significant ENAs from the outer magnetospheric regions. We infer that flow velocities in these regions should influence the emissions detected in the different energy bands. Inclusion of those velocities, which in this region can provide a large part of the ENA speed, has produced general agreement on the overall flux levels between the model results and data in some cases. However, there are also some significant differences, with the model showing little or no enhancement at the lower energy, in contrast to the IBEX ENA observations, which show strong enhancement at both energies shown. Perhaps the detailed flows present in the model led to discrepancies in the structure and brightness of the simulated ESA 3 emissions early in the event.

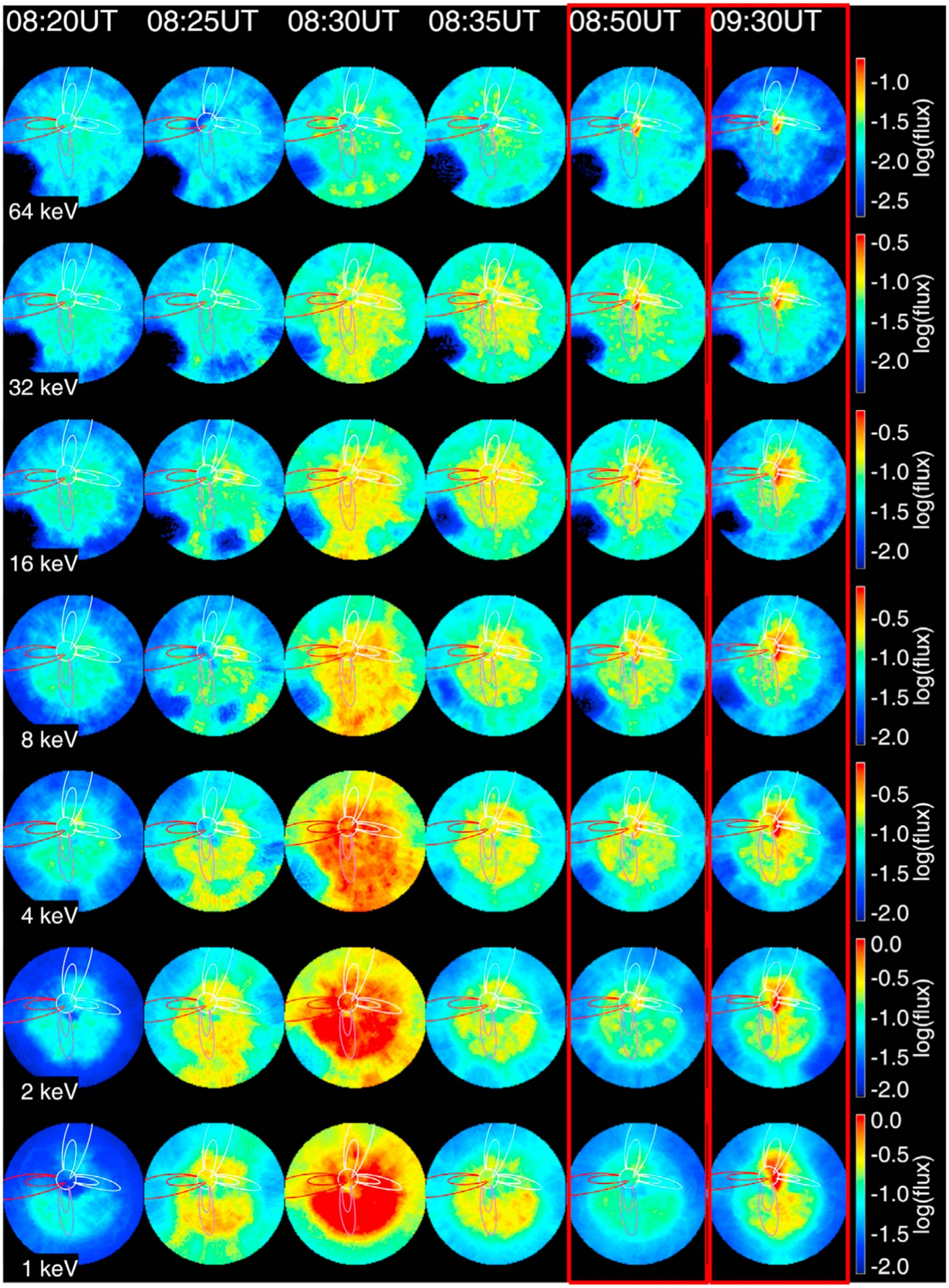
08:20UT
08:25UT
08:30UT
08:35UT
08:50UT
09:30UT
64 keV
32 keV
16 keV
8 keV
4 keV
2 keV
1 keV
log(flux)
-1.0
-1.5
-2.0
-2.5
-0.5
0.0

Figure 7

Table 2. TWINS Energy Bands and Approximate Observational Time Lags

$E_{Minimum}$ (keV)	E_{Nom} (keV)	$E_{Maximum}$ (keV)	Speed of H at E_{Nom} (km/s)	5 R_E Travel Time (s)
32	64	94	3520	9
16	32	48	2490	13
8	16	24	1760	18
4	8	12	1245	25
2	4	6	880	37
1	2	3	622	52
0.5	1	1.5	440	73

[20] We next examine simultaneous observations of magnetospheric ENAs from TWINS 1. In Figure 7, each column displays seven separate images, which collectively cover energies from 0.5 to 96 keV. Each image was produced from detailed information about the detection of individual ENAs. While TWINS data can be binned at any energy resolution, for these images we chose 100% wide energy bins as indicated in Table 2. Figure 7 comprises six sets of energy resolved images, each collected over five minutes of observations, with the start times of each shown at the top.

[21] In all images in Figure 7, we have first applied a process we call "statistical smoothing" (first introduced for analysis of IBEX heliospheric data [*McComas et al.*, 2009c] and subsequently adapted for TWINS data [*Valek et al.*, 2010]), where smoothing is performed on high-resolution data until a desired level of minimum statistical certainty (counting statistics) is reached for the entire image. Since then, we have continued to evolve and perfect the implementation of statistical smoothing of TWINS data. For this study, we use counts in individual $1^\circ \times 1^\circ$ pixels and sum with their neighbors until achieving at least 25 counts (corresponding to 20% Poisson statistics) in order to produce smoothed flux images. By this algorithm, portions of the original image that already had 25 counts were unsmoothed. Subsequently, we apply a newly developed background subtraction procedure that significantly improves the quality of the TWINS images when certain types of background are present in one of the two ENA head. Details of both statistical smoothing as we apply it to TWINS data and the background suppression procedure are provided in Appendix A.

[22] The 08:20–08:25 images in Figure 7 are very similar to other images over the preceding couple of hours. These represent the relatively quiet magnetospheric emissions prior to the interplanetary shock arrival. The 08:25–08:30 images cover the shock arrival and first few minutes thereafter. The 08:30–08:35 images are the brightest in the sequence with the emissions in the subsequent five minutes (08:35–08:40) showing significantly reduced ENA fluxes, especially at lower energies. Much of the apparent enhancement in the lower-energy 08:30–08:35 images, when the magnetosphere was initially compressed, is identifiable as background from

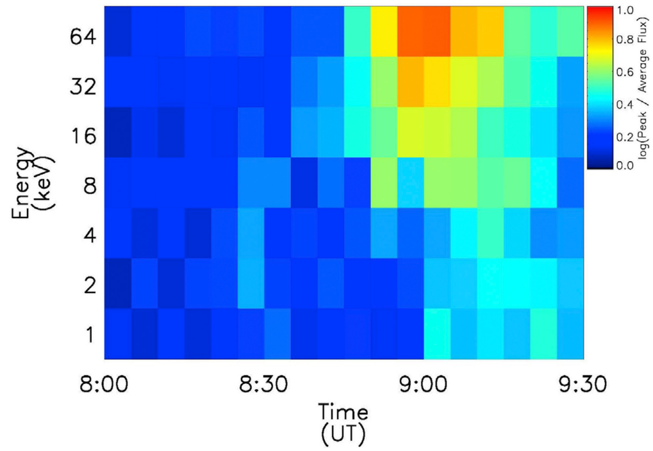

Figure 8. Color-coded ratio of peak to average ENA flux observed inside of 2 R_E geocentric distances. This ratio provides a qualitative assessment of the existence and strength of the LAE emission, which begin first at the highest energies ~15 min after the shock arrives and fill in at lower energies over the subsequent ~20 min.

higher-energy ions entering through the TWINS collimator (the collimators should remove all ions with energies less than ~7–10 keV) and particles penetrating the instrument walls (see appendix). In contrast, the higher-energy ring current emissions (>10 keV) continue to show enhanced emissions, very similar to the times of peak intensity for at least 20 min after the shock arrival. Finally, the fifth (08:50–08:55) and sixth (09:30–09:35) columns show the emissions roughly 20 min and an hour after the shock arrival, the latter being near the end of the substorm when the magnetosphere is again approaching a quieter magnetospheric state.

[23] Inspection of the individual sets of five minute averaged images from 08:40 to 09:30 show a consistent evolution with a slow decay in the ring current emissions at high altitudes and the growth of low-altitude emissions (LAEs) near the Earth. These LAEs are bright emissions produced by precipitating ring current ions that show up near the limb of the Earth under the correct viewing geometry; LAEs are routinely observed from both TWINS spacecraft [*McComas et al.*, 2009a; *Bazell et al.*, 2010; *Valek et al.*, 2010]. While none of the images show significant LAEs prior to or during the shock arrival (left four columns), the highest four energy bands show initial brightening of the LAEs by 08:50–08:55 (fifth column) and by 09:30–09:35 (last column), the LAEs show up as bright near-Earth emissions across all energies.

[24] Figure 8 shows the time evolution of the LAE enhancement from 08:00 to 09:30 UT as a function of energy. Plotted is the log of the ratio of the peak pixel to the average measured ENA flux (total flux divided by the number of pixels inside 2 R_E geocentric). While the statistical smoothing and background subtraction make the precise

Figure 7. Energy-resolved TWINS images of substorm ENA emissions sorted by time and energy. Each column shows a different set of 5 min integrated images, with the start time listed on the top. Each row of images shows a different energy band (central energies indicated on the left side), all of which have 100% energy resolution; each row also has a common three decade logarithmic color bar. The last two columns of images (indicated by red boxes) are from roughly 20 min and 1 h after the shock arrival. In all images, the Earth limb (white circle) and L = 4 and L = 8 model field lines are shown at noon (red) and at 6, 12, and 18 magnetic local time.

value of this ratio less important, the fact that the LAEs are so highly localized allows this ratio to provide a good qualitative indication of their relative strength. Dark blue regions of Figure 8 (log(ratio) < 0.3) indicate that essentially no LAEs are present; this was true at all energies until ∼08:45 UT, ∼15 min after the shock arrival. Starting at this time, the highest-energy LAEs show up with continued LAE brightening at higher energies and the onset of LAEs at progressively lower energies over the next ∼20 min.

[25] Just as for the IBEX observations, we have also produced simulated ENA images to compare with the TWINS observations. Again, the emissions arise from the line-of-sight integration of an optically thin source region (equation (2)). For this comparison, we calculated the 3-D distributions of ring current fluxes using the Comprehensive Ring Current Model (CRCM) [*Fok et al.*, 2001], which is an appropriate tool for studying ring current dynamics [*Fok et al.*, 2003; *Ebihara and Fok*, 2004; *Jones et al.*, 2006; *Fok et al.*, 2006; *Buzulukova et al.*, 2010; *Fok et al.*, 2010]. The CRCM solves the bounce-averaged Boltzmann equation to obtain the temporal evolution of phase space density for ring current ions. The CRCM calculates the Birkeland currents and electric field in the inner magnetosphere self-consistently with the ring current pressure distribution. The empirical T96 model [*Tsyganenko*, 1995; *Tsyganenko and Stern*, 1996] is used to provide the magnetospheric magnetic field. The polar boundary condition for the electric field potential is calculated from the Weimer-2000 convection model [*Weimer*, 2001]. The density and temperature of the plasma sheet are calculated with the empirical TM2003 model [*Tsyganenko and Mukai*, 2003] at r = 10 R_E. The CRCM outer boundary in the equatorial SM plane is located at r ∼ 9 R_E.

[26] Figure 9 shows the simulated images, which have been plotted over the exact same energy ranges and times, from the perspective of the TWINS spacecraft, and on the same color bars for each energy band. Thus, it is again straightforward to compare these images directly with the actual TWINS observations shown in Figure 7. The real data include additional noise and backgrounds, which show up as apparent emissions; these backgrounds are most evident in the lower-energy images from 08:30 UT but are also present at lower levels in the other images. Nonetheless, the overall levels of ENA fluxes emanating from the ring current are quantitatively quite similar to the observed levels. Note that this comparison can only be made for the higher-altitude, direct emissions from the ring current as the CRCM only simulates ring current fluxes and does not include ion precipitation and thus the capability to model LAEs.

[27] An interesting difference between the observed and simulated ENA images is that the simulated ones show relatively little variation with time over the interval shown with only a progressive brightening at nearly fixed local times and altitudes across each row of Figure 9. In contrast, the TWINS images in Figure 7 show significant intensification in the ring current from before to after the interplanetary shock arrival. It is likely that IPS- and substorm-related inductive electric fields can significantly contribute to ring current flux enhancements and corresponding enhancements in the ENA emissions. In this particular CRCM simulation, we used the dynamic T96 magnetic field model. The CRCM has inductive electric fields associated with changes in the T96 magnetic field, however, one can hardly expect an accurate description of IPS- and substorm-related changes in magnetic field geometry with the T96 model, especially for extreme cases like this event. A possible solution for this is to use a fully coupled CRCM-MHD model, which is currently being developed by the TWINS team. In any case, comparison of the model and direct observations indicate that the real ring current can be far more dynamic than even the best current model (CRCM) can predict.

3. Discussion

[28] This study is the first to combine two unique sets of magnetospheric ENA observations: (1) TWINS, which provides continuous ENA observations of the ring current and LAE emissions, with periodic stereo imaging from the two spacecraft, and (2) IBEX, which was designed to image the dim ENA emissions from the outer heliosphere but which also provides extremely sensitive observations of more distant portions of the Earth's magnetosphere. Together TWINS and IBEX have provided a unique and simultaneous imaging of the Earth's magnetosphere and enabled the first truly global perspective of a magnetospheric substorm: the 5 April 2010 substorm that led to the loss of control of Intelsat's Galaxy 15 communications satellite in geosynchronous orbit.

[29] The 5 April 2010 substorm was driven by a fast interplanetary shock that passed the Geotail spacecraft at ∼08:25 UT, approximately 15 R_E upstream from the Earth [*Connors et al.*, 2011], and thus arrived at and began compressing the magnetopause at ∼08:26 UT. Essentially immediately (between 08:26:08 and 08: 26:26 UT) this compressed region produced strongly enhanced ENA emissions that were observed several minutes later at IBEX ∼27 R_E off to the side of the Earth-Sun line, owing to the finite travel times of the ENAs at various energies.

[30] It is interesting that the subsolar magnetosheath ENA emissions observed by IBEX were immediately and strongly enhanced as soon as the interplanetary shock arrived. In addition, the background in the observations at the TWINS spacecraft increased essentially simultaneously (beginning between 08:25 and 08:30), and the ring current emissions were enhanced and stayed enhanced starting with the compression of the magnetosphere. At this juncture, it is not clear what mechanism associated with the shock arrival directly causes the ring current intensification. Perhaps it is simply compression of the magnetosphere reducing the flux tube volumes and increasing the ring current densities and emissions. On the other hand, it could be some other process. For example, adiabatic heating followed by pitch angle scattering through interactions with EMIC waves might explain such compression-related enhancements of magnetospheric ENA emissions.

[31] In contrast to the direct ring current emissions, the observed LAEs were significantly delayed, only beginning to show enhancements at the highest energies ∼15 min after the shock arrival. The subsequent LAE emissions observed by TWINS at progressively lower energies over the next ∼20 min indicate an interesting delay, which cannot simply be explained by ion dispersion and propagation times from the ring current down to the ionosphere. These times are much shorter and should only be one to a few minutes, even

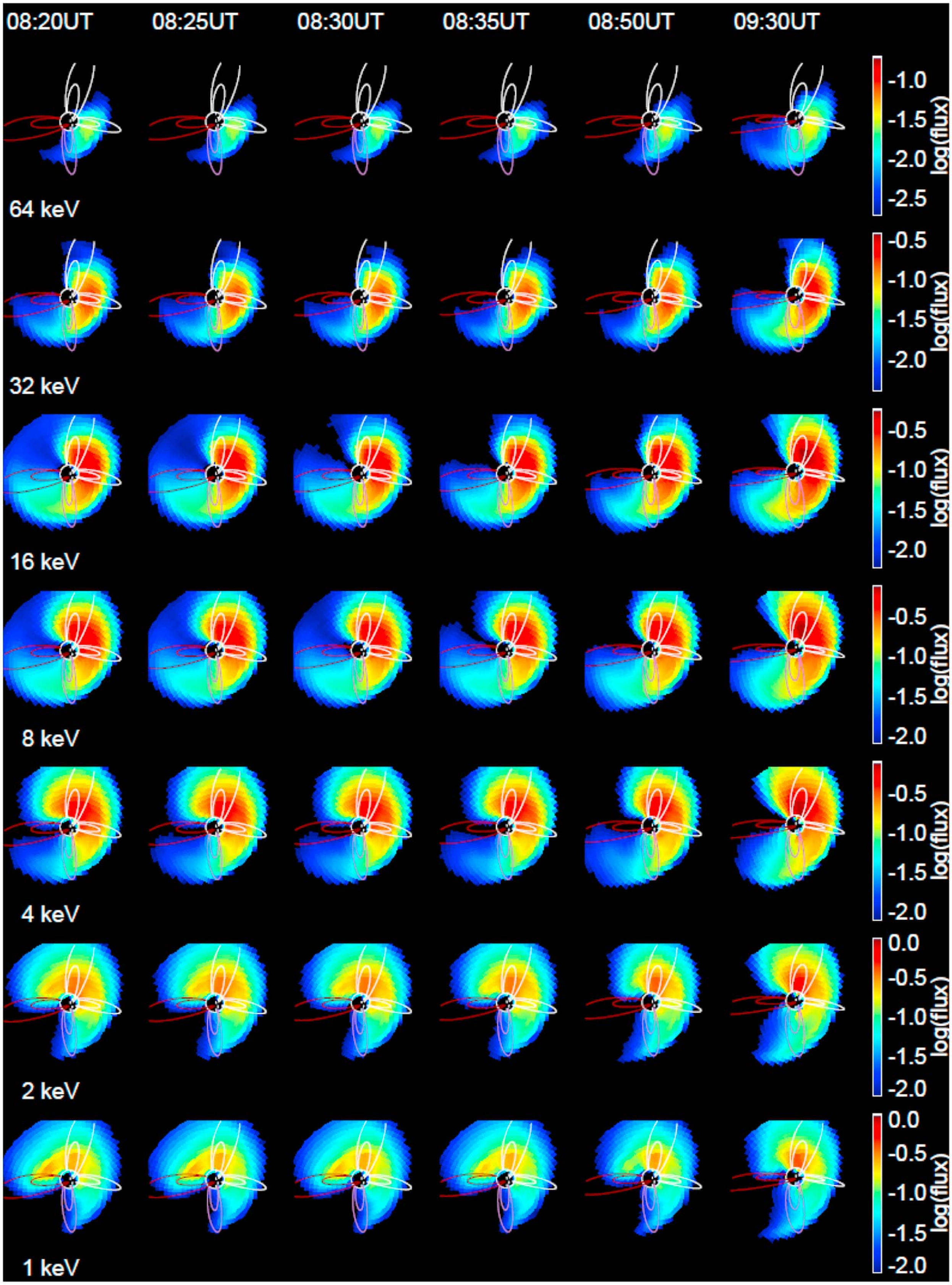

Figure 9. Simulation results covering the same times and energies as the TWINS observations and plotted using the same color bars and other features as those used in Figure 7 to facilitate direct comparison of the two sets of images.

down at 1 keV. Furthermore, the ENA propagation times once they are produced ~5 R_E from the TWINS spacecraft are all less than about one minute (see Table 2). Thus, the longer, tens-of-minutes time scale seems to represent evolution of the ring current pitch angle distribution toward the loss cone as ions precipitate.

[32] Another interesting aspect of the TWINS LAE emissions is that they are very bright at the highest energies observed even though the direct ring current emissions both observed at the same energies by TWINS and predicted by the CRCM model peak at lower energies. This combination of observations suggests that the LAEs are not simply a measure of the total ion content of various magnetic flux tubes in the ring current, but rather that some physical process "gates" the precipitation of ions down into the ionosphere where the LAEs are produced (it is also possible that there is some time-dependent complexity of the ENA production in the ionosphere). Since the viewing geometry changed relatively little over the observations shown here, we suggest that the strong global compression of the magnetosphere documented by IBEX likely changed both the drift paths of the ring current ions and altered which pitch angles were able to precipitate. For example, strong compressions are believed to produce pitch angle anisotropy in trapped magnetospheric ions [e.g., *Anderson and Hamilton*, 1993], which in turn generates ion cyclotron waves that pitch angle scatter (and thus enhance the precipitation of) ring current ions, with a broader range of pitch angle being affected for higher-energy particles [e.g., *Jordanova et al.*, 1997].

[33] In addition to the detailed timing and overall flux measurements provided by both IBEX and TWINS, the energy-resolved ENA measurements provide important spectral information about the emitting source regions. For example, Figure 4 shows that the preshock cusp emissions are significantly different from the compressed magnetosheath emissions after the interplanetary shock arrives, which are significantly enhanced at energies >1 keV compared to lower energies. This higher-energy enhancement increases through the peak ENA fluxes and stays enhanced even after the lower-energy fluxes have dropped back essentially to their preshock levels. Such a sequence is generally consistent with the much higher solar wind speed persisting after the arrival of the interplanetary shock, although an explanation of the detailed evolution of the ENA fluxes and spectra are beyond our current understanding of the magnetospheric system. At higher energies, TWINS observes a similar energy-dependent response in the ENA emissions from the trapped ring current. As already noted above, the >10 keV TWINS images continue to show enhanced emissions well after the initial shock arrival, and well beyond the brief background enhancement caused by direct particle penetration. Thus, spectral information in ENA images provides an essential window into the processes whereby the solar wind inputs energy into the magnetosphere.

[34] The combined IBEX and TWINS observations provide a more complete global picture of the complicated magnetospheric evolution than has ever been available before. In order to address these more detailed connections, this study also provides simulated ENA fluxes for comparison with both the IBEX and TWINS observations. The simulations were run as if viewing from the actual locations of the IBEX and TWINS spacecraft, cover the same integration times as the observations, and were plotted on exactly the same color bars as the data. In general, the observed and predicted fluxes are similar, with similar peak flux values. However, the detailed distributions, time evolution, and energy distribution do differ between the IBEX and TWINS observations and their respective simulations.

[35] ENA emission imaging and MHD simulations both have a global nature, and intercomparison allows a check on the validity of the simulations, and aids in interpretation of the data. Furthermore, sometimes what is not shown is also important. For example, the MHD simulation of the IBEX observations prior to the arrival of the interplanetary shock failed to show the cusp emissions, but did show time-variable fast flows from near the nose. Similarly, the simulations of the TWINS data showed far less variability in the predicted ENA fluxes over this substorm event than actually observed. Such differences demonstrate the potential to directly extract information about plasma flows and enhancements, using multienergy ENA detectors of sufficient sensitivity; comparison of such observations should allow testing and improvements to the current set of MHD models and provide for much deeper and more detailed physical understanding of the magnetosphere.

Appendix A

[36] This appendix documents several important details of the TWINS data analysis that have been developed since the original TWINS mission paper [*McComas et al.*, 2009a]. In particular, we describe and document our method for binning the ENA data (section A1), a recently developed process called "statistical smoothing" that was first used for ENA imaging of the outer heliosphere on IBEX [*McComas et al.*, 2009b] (section A2), and our method for differential background subtraction between TWINS ENA heads (section A3). This appendix is intended to provide the detailed explanation and citable reference for these advanced analysis tools as they are currently applied to TWINS images.

A1. ENA Binning

[37] The TWINS instruments [*McComas et al.*, 2009a] produce 3-D ENA images (two spatial dimensions and one velocity dimension) by combining measurements from two separate ENA sensor heads. The sensor heads are referred to as the AWAY head of the TOWARD heads. This naming convention specifies the head look direction with respect to the instrument electronics box.

[38] The approximate FOV for each sensor is indicated in Figure A1. Each sensor head makes an instantaneous image over 1 spatial dimension and velocity space. The whole instrument is then actuated back and forth in a windshield wiper motion to fill in the second spatial dimension. The TWINS data are binned into 4° wide actuation sectors. With a nominal actuation velocity of 3° s^{-1}, these data are accumulated over 1.333 s. A full sweep is made up by combining 45 sectors to get 180° of actuation. A full sweep is 60 s of data plus an additional 12 s of time required to reverse the motion of the actuator. Therefore, a 60 s image is produced every 72 s. Figure A1 shows this process schematically. The

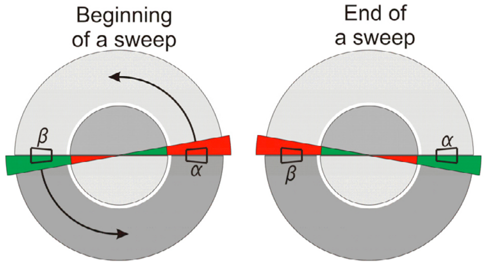

Figure A1. Schematic of the sensor head FOVs. Images are generated by sweeping the ~1-D FOV in a windshield wiper motion. The approximate instantaneous FOV for the TOWARD (AWAY) head is shown in red (green). The total FOV after a full sweep of the actuator for the TOWARD (AWAY) sensor head is shown in light (dark) gray. At the end of every other sweep the two sensor heads are looking in approximately the same direction.

instantaneous FOV for the AWAY (TOWARD) sensor head is shown in green (red), and the FOV for a full sweep is the region shaded dark (light) gray. Images are created by using an integer number of sweeps.

[39] TWINS uses coincidence measurements to determine each particle's Time of Flight (TOF) and for background rejection. For each sector the data include 16 bit counters for the total number of valid events by sensor head and detailed information for up to the first 1253 valid events from both heads. This detailed information, called the Direct Events (DEs) includes information to determine the incident angle, particle TOF, and a time "slice" that increments every 1/3 s. With the constant actuation velocity, the slice value defines the actuation position to 1°.

[40] During times of high counting rates, the total number of valid events may exceed the allotted telemetry for DEs. For each sector of data there is enough telemetry to report only up to the first 1253 DEs. Since for each sector the telemetry gets filled in chronological order, we can use the slice information to estimate the time used to acquire DEs. If there is at least 1 DE reported in slice n, and slice n is the last slice in a sector with any DEs, then we know that there was sufficient telemetry for all DEs measured in the previous slices. For those 1° wide slices the DEs were accumulated over a full 1/3 s. We can determine the total number of valid events that are in slices n through the end of the sector as the difference of the total valid events and the total DEs in the slices prior to slice n. Making the assumption that the remaining valid events are uniformly distributed over slices n through end of the sector, then we can estimate what fraction of the DEs were not available for transmission for slice n, and scale the accumulation time appropriately.

[41] The TWINS sensors measure the incident direction of the ENAs and the TOF of the ENAs inside the sensor to determine the particles velocity. The DEs are binned by incident angle and TOF. Both of these quantities have uncertainty due to the interaction of the incident ENA with the thin carbon foil of the instrument [*McComas et al.*, 2004, 2009a; *Valek et al.*, 2010, and references therein] and from the finite width of the bins used for the angle and TOF. The particles energy is calculated from the velocity (path traveled in the sensor determined from incident angle divided by the TOF) and mass, here assumed to be H.

[42] Since both incident angle and TOF are measured in discreet bins, the resultant energy bins boundaries are not constant over the full FOV; that is, the determined energy from TOF bin i will be different at angle bin j and bin $j + 1$. Figure A2 shows the effect of the discreet TOF binning has on the energy bands over a small angular range. The alternating blue and orange bars are for different TOF bins and the horizontal black lines indicate the limits of the 32 keV energy band used in this paper. The limits of the 32 keV energy band in general do not line up with the boundaries imposed by the discreet TOF bins.

[43] In order to make a meaningful image for a given energy, we must address how the discreet energy binning varies with angle. The similar IMAGE MENA instrument [*Pollock et al.*, 2000] uses the method of *Henderson et al.* [2005] in which a fit to the measured energy spectra for each angle bin is used to determine the flux at a given energy. This was necessary for MENA owing to its limited telemetry for TOF.

[44] TWINS has a TOF resolution that is 4 times finer than that of MENA, so a more direct approach can be used. To account for the variation in the TWINS energy bins as a function of angle, the counts per energy and angle band will include the counts from the discreet energy bins that fully fit in the larger array (e.g., 16–48 keV), and a fraction of counts from the bins that straddle the boundaries in the full energy bin. A simple linear interpolation using the TOF bin that straddles the energy bin boundary and the last TOF bin that is completely inside the energy bin boundary is used to estimate the fraction of counts to include from the partial TOF bins.

A2. Statistical Smoothing

[45] The TWINS images typically cover a large dynamic range, with the locally intense LAE being orders of magnitude brighter than the more diffuse High-Altitude Emissions

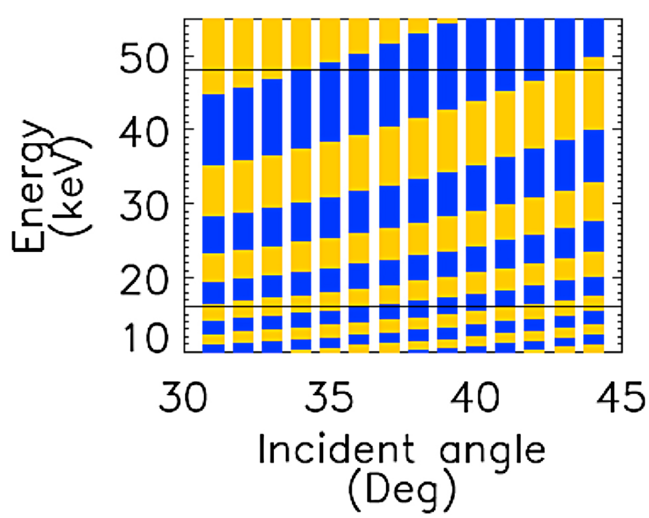

Figure A2. The energy binning due to finite TOF bin resolution. For a constant incident angle, the alternating blue and orange colors indicate the energy band for a single TOF value. The lines at 16 and 48 keV show the limits of our 32 keV energy band used in this paper.

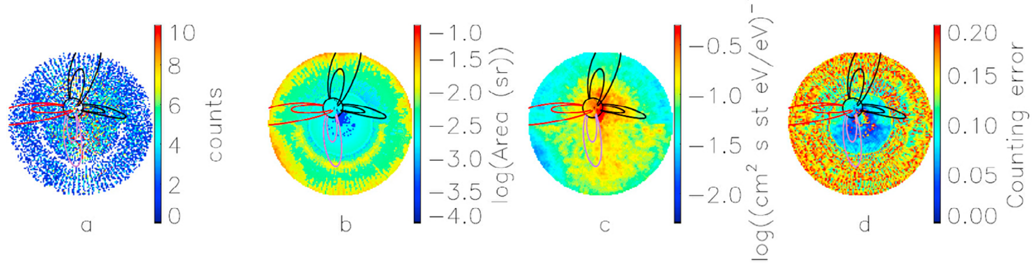

Figure A3. Illustration of the statistical smoothing process. (a) The total number of counts per pixel before any instrument response functions or dynamic smoothing has been applied. (b) The area (in steradians) that must be included for each pixel to achieve the target value of 25 counts. (c) The image that has been created after the statistical smoothing and proper instrument response functions have been applied. (d) The error in the image due to counting statistics. The data in Figure A3 is from the 16 keV energy band at 09:00 UT on 5 April 2010.

(HAE). Also the sensitivity of the TWINS sensors varies with imaging angle, which leads to variation of the measured counts across an image of even relatively uniform ENA flux. The error due to counting statistics therefore can vary significantly across an image. To maintain a more uniform error from counting statistics across an image, we developed an image processing technique we call "Statistical Smoothing."

[46] In this process counts from surrounding pixels are summed to achieve a minimum error from counting statistics. The size of the region of included pixels varies dynamically to maintain the minimum number of counts per pixel. This can be thought of a sliding boxcar average where the width of the boxcar can change from step to step to maintain a minimum error. This has the virtue of maintaining high spatial resolution in regions of high flux (e.g., locally intense LAE) and having sufficient counts in regions of low flux (e.g., diffuse HAE). The statistical smoothing method requires the least amount of smoothing needed to achieve any particular statistical certainty. This statistical smoothing method was invented and first used by *McComas et al.* [2009b] for ENA imaging of the outer heliosphere with IBEX and was subsequently extended to handle TWINS ENA images of the inner magnetosphere [*Valek et al.*, 2010].

[47] The TWINS images shown in this paper have been processed to have at least 25 counts (20% Poisson counting statistics) in each pixel. If the counts in a given pixel are less than this specified target value, counts from the surrounding nearest neighbors are added until the target value is reached. When this target value is reached, the new counts total and commensurate geometric factor are then recorded for that pixel in a new array. The counts and geometric factor over the region of contributing pixels are combined to calculate the correct intensity. In regions of the image with high counts, just the original single pixel or only a small area around that pixel is needed to reach the target value, while in regions of low counts the areas can include many adjacent initial pixels.

[48] The pixels with a FOV closest to parallel to the rotation axis sweep out a smaller solid angle than pixels at the outer edge of the image. For statistical smoothing, we derive regions that are approximately square in solid angle viewing as opposed to being "equal" in instrument angle coordinates. The regions of approximately square solid angle are 1° wide in the instrument imaging direction (radial in the images) by *m* degrees wide in the instrument actuation direction (azimuthal in the images). The value of *m* is determined to give the new pixel a solid angle that is approximately that of a 1° × 1° pixel 55° from the center of the image. The value of *m* is constrained to be an odd integer value so that the averages are centered on the pixel.

[49] Figure A3 shows the steps in the dynamic smoothing process. Shown in Figure A3a is the total number of counts per 1° × 1° pixel before any instrument response functions or dynamic smoothing has been applied. The white space indicates pixels where no DEs are returned either owing to low sensitivity for that particular look direction or owing to telemetry limitations preventing the measurement being transmitted. Figure A3b shows the area of pixels that must be included for each pixel to achieve the target value of 25 counts. The TWINS instrument has a region of low sensitivity that can be seen as a semicircle in the lower half of the images. This can be seen as the absence of counts in Figure A3a and as the increase of required area to reach the target value in Figure A3b. Figure A3c shows the image that has been created after statistical smoothing and proper instrument response functions have been applied. Figure A3d shows the error in the image due to counting statistics.

[50] The amount of smoothing is determined by the target value. Figure A4 shows the effect on the image when the target value is increased. In each image, the solid angle required to meet or exceed the target value is shown as the image on the top, and the resultant smoothed image is shown on the bottom for the same time period and energy shown in Figure A3. The target values used were 0, 9, 25, and 100. Since Poisson statistical errors go as the square root of the number, the per pixel maximum errors are 33%, 20%, and 10% in Figures A4b, A4c, and A4d, respectively. A target value of 0 results in no smoothing except for the center of the image. A target value of 25 counts provides a reasonable error (20%) and produces quality images without lengthy processing (processing time is a function of the target value). Note in Figure A4 that there is little difference between the 25 and 100 count images. At the center of the image 1°×1° pixels are combined to maintain approximately equal solid angle bins. The steps seen in the solid angle plots for Figure A4a are a result of the constraint that

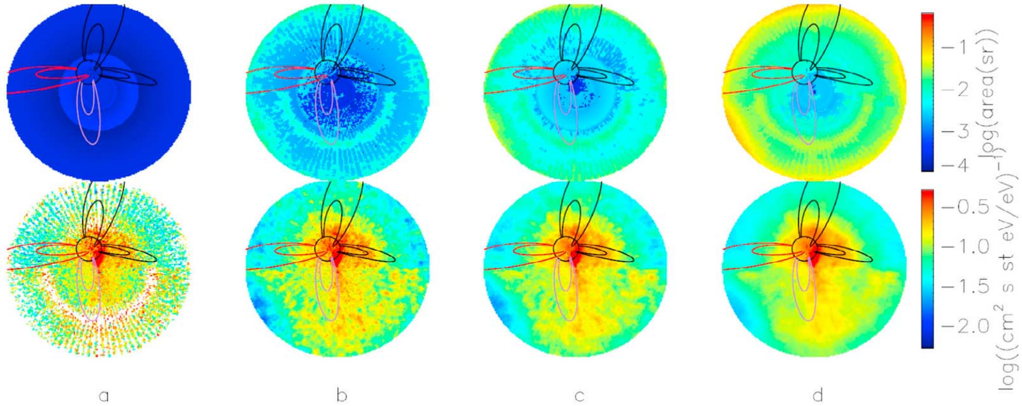

Figure A4. Illustration of the effect the target value has on images for target values of (a) 0 counts, (b) 9 counts, (c) 25 counts, and (d) 100 counts. Bottom images are of the ENA flux after statistical smoothing has been applied, and top images are of the total area per pixel required to reach the target levels.

m (number of bins in the azimuthal direction) be an odd integer.

A3. Background Subtraction

[51] There are times when the sensitive TWINS ENA sensors have backgrounds that are comparable to the ENA signal. TWINS is sensitive to three classes of backgrounds; UV light, penetrating energetic particles that can pass through the instrument walls, and medium energy charged particles, which are energetic enough to pass through ion rejection collimators. UV from the Earth and the geocorona are effectively attenuated by freestanding transmission gratings (transmission $\sim$0.6 $\times$ 10^{-5}) [*McComas et al.*, 2009a]. The Ly-α from the Sun is intense enough to pass through the freestanding transmission gratings; however, the Sun is typically not within the FOV of TWINS. Sectors of data that have the Sun within 20 degrees of its FOV are removed from the images. (No images in this paper met this criterion and needed to be removed.)

[52] Penetrating energetic particles pass through the walls of the sensor, and therefore do not produce valid events. However, during periods of high fluxes penetrating particle false coincident events are possible. These false "valid" events are identified by their isotropic distribution. TWINS is turned off as it enters perigee to prevent this sort of contamination from the radiation belts.

[53] The TWINS sensors use charged-particle-rejection collimators to suppress the background from medium energy charged particles in the local environment. The TWINS sensors use charged-particle-rejection collimators to suppress this background. The collimators are constructed with a series of parallel plates that have high voltage applied to every other plate, with the remaining plates held at ground. The resultant electric field between these plates is to sweep out charged particles [*McComas et al.*, 2009a].

[54] The high voltage applied to these collimator plates dropped and then stabilized over the first year of the mission. Currently the voltage levels are such that the TWINS1 AWAY sensor head is lower than that for the TWINS1 TOWARD head. The lower voltage applied to the AWAY sensor head make it more susceptible to charged particle penetration through its collimator. The effect of this background is the apparent increased flux seen in the AWAY sensor head in Figures A3 and A4. (See Figure A1 for the AWAY and TOWARD sensors FOV.)

[55] The images in this paper were made of multiple sweeps (four sweeps), and therefore the measured flux at the end of the sweeps seen in either head should be nearly identical if we assume the ENA flux varies slowly over an $\sim$5 min image. The similar look directions for the sensor

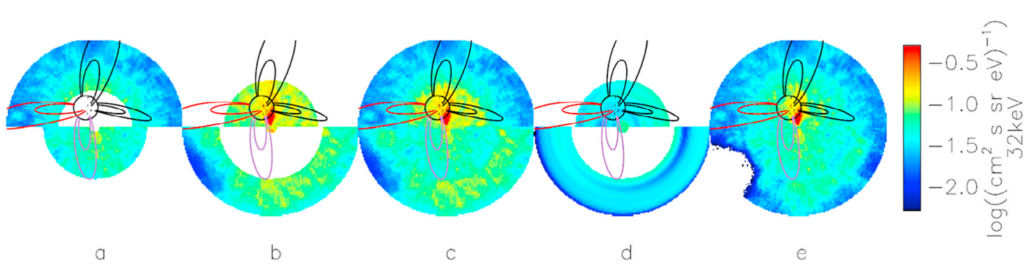

Figure A5. Demonstration of the background subtraction. (a) The image created using only the TOWARD sensor head. (b) The image created using only the AWAY sensor head. (c) The complete (two-sensor) image that results from combining data from these two different heads. (d) The flux difference map used to remove the excess background in the AWAY head. (e) The background subtracted flux map.

heads are shown schematically in Figure A1. The regions labeled α and β are sampled by both the TOWARD head (red wedge) and the AWAY head (green wedge). The difference in the measured flux at the ends of the sweep then gives a measure of the excess backgrounds seen in the AWAY head. The difference between the red and green curves at each end of the actuation cycle is linear interpolated over the actuation angle to estimate the angular dependence of the background.

[56] Figure A5 illustrates the steps of this process. Figure A5a (Figure A5b) is an image generated using only the data from the TOWARD (AWAY) sensor head, and the combined image is in Figure A5c. The excess background in the AWAY sensor head with the linear interpolation applied is shown in Figure A5d. This map of the flux differences is then converted to counts using the instrument response functions and subtracted from the raw counts image. The statistical smoothing process is then applied using the background subtracted counts to generate the image shown in Figure A5e. All images shown in the body of the paper have this background subtraction applied.

[57] This process removes excess background from the AWAY sensor head but does not address any backgrounds that are common to both sensor heads. Also if there are sharp spatial gradients at the location where the differences are determined this process can return unreliable results. The largest spatial gradients are typically at the location of the LAEs. For the time period covered in this paper, the LAEs are far enough from the region where the background subtraction is performed to allow for a good background subtraction.

[58] **Acknowledgments.** We are deeply indebted to all of the outstanding men and women who have made both the IBEX and TWINS missions such great successes, and we specifically thank R. Vanderspek for help with the data processing and S. Petrinec for help with Figure 3. We also thank the ACE and Wind plasma and magnetometer teams for L1 data and the OMNI data set for their propagation of these data. Simulation results were provided by the Community Coordinated Modeling Center at GSFC (http://ccmc.gsfc.nasa.gov) using the Open GGCM Model developed by J. Raeder. This work was supported by the IBEX and TWINS missions as a part of NASA's Explorer Program.

[59] Philippa Browning thanks J. Perez and another reviewer for their assistance in evaluating this paper.

References

Anderson, B. J., and D. G. Hamilton (1993), Electromagnetic ion cyclotron waves stimulated by modest magnetospheric compressions, *J. Geophys. Res.*, *98*, 11,369–11,382, doi:10.1029/93JA00605.

Bazell, D., E. Roelof, T. Sotirelis, P. Brandt, H. Nair, P. Valek, J. Goldstein, and D. McComas (2010), Comparison of TWINS images of low-altitude emission of energetic neutral atoms emissions with DMSP precipitating ion fluxes, *J. Geophys. Res.*, *115*, A10204, doi:10.1029/2010JA015644.

Buzulukova, N., M.-C. Fok, J. Goldstein, P. Valek, D. J. McComas, and P. C. Brandt (2010), Ring current dynamics in modest and strong storms: Comparative analysis of TWINS and IMAGE/HENA data with CRCM, *J. Geophys. Res.*, *115*, A12234, doi:10.1029/2010JA015292.

Connors, M., C. T. Russell, and V. Angelopoulos (2011), Magnetic flux transfer in the 5 April 2010 Galaxy 15 substorm: An unprecedented observation, *Ann. Geophys.*, *29*, 619–622, doi:10.5194/angeo-29-619-2011.

Ebihara, Y., and M.-C. Fok (2004), Postmidnight storm-time enhancement of tens-of-keV proton flux, *J. Geophys. Res.*, *109*, A12209, doi:10.1029/2004JA010523.

Fok, M.-C., R. A. Wolf, R. W. Spiro, and T. E. Moore (2001), Comprehensive computational model of Earth's ring current, *J. Geophys. Res.*, *106*, 8417–8424, doi:10.1029/2000JA000235.

Fok, M.-C., et al. (2003), Global ENA image simulations, *Space Sci. Rev.*, *109*, 77–103, doi:10.1023/B:SPAC.0000007514.56380.fd.

Fok, M.-C., T. E. Moore, P. C. Brandt, D. C. Delcourt, S. P. Slinker, and J. A. Fedder (2006), Impulsive enhancements of oxygen ions during substorms, *J. Geophys. Res.*, *111*, A10222, doi:10.1029/2006JA011839.

Fok, M.-C., N. Buzulukova, S.-H. Chen, P. W. Valek, J. Goldstein, and D. J. McComas (2010), Simulation and TWINS observations of the 22 July 2009 storm, *J. Geophys. Res.*, *115*, A12231, doi:10.1029/2010JA015443.

Fuselier, S. A., et al. (2010), Energetic neutral atoms from the Earth's subsolar magnetopause, *Geophys. Res. Lett.*, *37*, L13101, doi:10.1029/2010GL044140.

Grimes, E. W., J. D. Perez, J. Goldstein, D. J. McComas, and P. Valek (2010), Global observations of ring current dynamics during CIR-driven geomagnetic storms in 2008, *J. Geophys. Res.*, *115*, A11207, doi:10.1029/2010JA015409.

Henderson, M. G., M. F. Thomsen, R. Skoug, M. H. Denton, R. Harper, H. O. Funsten, and C. J. Pollock (2005), Calculation of the IMAGE/MENA geometric factors and conversion of images to units of integral and differential flux, *Rev. Sci. Instrum.*, *76*, A043303, doi:10.1063/1.1884190.

Jones, S. T., M.-C. Fok, and P. C. Brandt (2006), Modeling global O+ substorm injection using analytic magnetic field model, *J. Geophys. Res.*, *111*, A11S07, doi:10.1029/2006JA011607.

Jordanova, V., J. Kozyra, A. Nagy, and G. Khazanov (1997), Kinetic model of the ring current-atmosphere interactions, *J. Geophys. Res.*, *102*, 14,279–14,291, doi:10.1029/96JA03699.

Keesee, A., N. Buzulukova, J. Goldstein, D. J. McComas, E. E. Scime, H. Spence, and K. Tallaksen (2011), Remote observations of ion temperatures in the quiet time magnetosphere, *Geophys. Res. Lett.*, *38*, L03104, doi:10.1029/2010GL045987.

Lee, D.-Y., S. Ohtani, P. C. Brandt, and L. R. Lyons (2007), Energetic neutral atom response to solar wind dynamic pressure enhancements, *J. Geophys. Res.*, *112*, A09210, doi:10.1029/2007JA012399.

Lindsay, B. G., and R. F. Stebbings (2005), Charge transfer cross sections for energetic neutral atom data analysis, *J. Geophys. Res.*, *110*, A12213, doi:10.1029/2005JA011298.

McComas, D. J., F. Allegrini, C. J. Pollock, H. O. Funsten, S. Ritzau, and G. Gloeckler (2004), Ultra-thin (~10 nm) carbon foils in space instrumentation, *Rev. Sci. Instrum.*, *75*, 4863–4870, doi:10.1063/1.1809265.

McComas, D. J., et al. (2009a), The Two Wide-Angle Imaging Neutral-Atom Spectrometers (TWINS) NASA Mission-of-Opportunity, *Space Sci. Rev.*, *142*, 157–231, doi:10.1007/s11214-008-9467-4.

McComas, D. J., et al. (2009b), IBEX: Interstellar Boundary Explorer, *Space Sci. Rev.*, *146*, 11–33, doi:10.1007/s11214-009-9499-4.

McComas, D. J., et al. (2009c), Global observations of the interstellar interaction from the Interstellar Boundary Explorer (IBEX), *Science*, *326*, 959–962, doi:10.1126/science.1180906.

McComas, D. J., H. O. Funsten, S. A. Fuselier, W. S. Lewis, E. Möbius, and N. A. Schwadron (2011a), IBEX observations of heliospheric energetic neutral atoms: Current understanding and future directions, *Geophys. Res. Lett.*, *38*, L18101, doi:10.1029/2011GL048763.

McComas, D. J., et al. (2011b), First IBEX observations of the terrestrial plasma sheet and a possible disconnection event, *J. Geophys. Res.*, *116*, A02211, doi:10.1029/2010JA016138.

Möstl, C., M. Temmer, T. Rollett, C. J. Farrugia, Y. Liu, A. M. Veronig, M. Leitner, A. B. Galvin, and H. K. Biernat (2010), STEREO and Wind observations of a fast ICME flank triggering a prolonged geomagnetic storm on 5–7 April 2010, *Geophys. Res. Lett.*, *37*, L24103, doi:10.1029/2010GL045175.

Petrinec, S. M., et al. (2011), Neutral atom imaging of the magnetospheric cusps, *J. Geophys. Res.*, *116*, A07203, doi:10.1029/2010JA016357.

Pollock, C. J., et al. (2000), Medium Energy Neutral Atom (MENA) Imager for the IMAGE Mission, *Space Sci. Rev.*, *91*, 113–154, doi:10.1023/A:1005259324933.

Raeder, J., R. L. McPherron, L. A. Frank, S. Kokubun, G. Lu, T. Mukai, W. R. Paterson, J. B. Sigwarth, H. J. Singer, and J. A. Slavin (2001), Global simulation of the Geospace Environment Modeling substorm challenge event, *J. Geophys. Res.*, *106*, 381–395, doi:10.1029/2000JA000605.

Rairden, R. L., L. A. Frank, and J. D. Craven (1986), Geocoronal imaging with Dynamics Explorer, *J. Geophys. Res.*, *91*, 13,613–13,630, doi:10.1029/JA091iA12p13613.

Rossi, B., and S. Olbert (1970), *Introduction to the Physics of Space*, McGraw-Hill, New York.

Singer, H. J., et al. (2010), Multipoint observations of the large substorm associated with the Galaxy 15 anomaly, Abstract SM22B-05 presented at 2010 Fall Meeting, AGU, San Francisco, Calif., 13–17 Dec.

Tsyganenko, N. A. (1995), Modeling the Earth's magnetospheric magnetic field confined within a realistic magnetopause, *J. Geophys. Res.*, *100*, 5599–5612, doi:10.1029/94JA03193.

Tsyganenko, N. A., and T. Mukai (2003), Tail plasma sheet models derived from Geotail particle data, *J. Geophys. Res.*, *108*(A3), 1136, doi:10.1029/2002JA009707.

Tsyganenko, N. A., and D. P. Stern (1996), Modeling the global magnetic field of the large-scale Birkeland current systems, *J. Geophys. Res.*, *101*, 27,187–27,198, doi:10.1029/96JA02735.

Valek, P., P. C. Brandt, N. Buzulukova, M.-C. Fok, J. Goldstein, D. J. McComas, J. D. Perez, E. Roelof, and R. Skoug (2010), Evolution of low altitude and ring current ENA emissions from a moderate magnetospheric storm: Continuous and simultaneous TWINS observations, *J. Geophys. Res.*, *115*, A11209, doi:10.1029/2010JA015429.

Weimer, D. R. (2001), An improved model of ionospheric electric potentials including substorm perturbations and application to the Geospace Environment Modeling November 24, 1996, event, *J. Geophys. Res.*, *106*, 407–416, doi:10.1029/2000JA000604.

N. Buzulukova, CRESST, NASA Goddard Space Flight Center, Greenbelt, MD 20770, USA.

M. G. Connors, Department of Physics and Astronomy, Athabasca University Geophysical Observatory, Athabasca University, Athabasca, AB T9S 3A3, Canada.

M. A. Dayeh, S. Fuselier, J. Goldstein, D. J. McComas, and P. Valek, Southwest Research Institute, San Antonio, TX 78228, USA. (dmccomas@swri.edu)

H. O. Funsten, Los Alamos National Laboratory, Los Alamos, NM 87545, USA.

N. A. Schwadron, Department of Physics, University of New Hampshire, Durham, NH 03824, USA.